arXiv:1203.5929v2 [astro-ph.CO] 30 Jun 2012

Imaging Simulations of the Sunyaev-Zel'dovich Effect for ALMA

Kenkichi Yamada[1], Tetsu Kitayama[1], Shigehisa Takakuwa[2], Daisuke Iono[3], Takahiro Tsutsumi[4],
Kotaro Kohno[5,6], Motokazu Takizawa[7], Kohji Yoshikawa[8], Takuya Akahori[9], Eiichiro Komatsu[10],
Yasushi Suto[6,11,12], Hiroshi Matsuo[13], and Ryohei Kawabe[3,13,14]

[1]*Department of Physics, Toho University, Funabashi, Chiba 274-8510, Japan*
[2]*Academia Sinica Institute of Astronomy and Astrophysics, P.O. Box 23-141, Taipei 10617, Taiwan*
[3]*Nobeyama Radio Observatory, Minamimaki, Minamisaku, Nagano 384-1305, Japan*
[4]*National Radio Astronomy Observatory, Socorro, NM 87801-0387, USA*
[5]*Institute of Astronomy, University of Tokyo, 2-21-1 Osawa, Mitaka, Tokyo 181-0015, Japan*
[6]*Research Center for the Early Universe, School of Science, The University of Tokyo, Tokyo 113-0033, Japan*
[7]*Department of Physics, Yamagata University, Kojirakawa-machi 1-4-12, Yamagata 990-8560, Japan*
[8]*Center for Computational Sciences, University of Tsukuba, 1-1-1, Tennodai, Ibaraki 305-8577, Japan*
[9] *Korea Astronomy and Space Science Institute, Daedeokdaero 776, Yuseong, Daejeon 305-348, Korea*
[10]*Texas Cosmology Center and Department of Astronomy, The University of Texas at Austin, Austin, TX 78712, USA*
[11]*Department of Physics, The University of Tokyo, Tokyo 113-0033, Japan*
[12]*Department of Astrophysical Sciences, Princeton University, Princeton, NJ 08544, USA*
[13]*National Astronomical Observatory of Japan, 2-21-1 Osawa, Mitaka, Tokyo 181-8588, Japan*
[14]*Joint ALMA Observatory, Alonso de Cordova 3107 OFC 129, Vitacura, Chile*

Abstract

We present imaging simulations of the Sunyaev-Zel'dovich effect of galaxy clusters for the Atacama Large Millimeter/submillimeter Array (ALMA) including the Atacama Compact Array (ACA). In its most compact configuration at 90GHz, ALMA will resolve the intracluster medium with an effective angular resolution of 5 arcsec. It will provide a unique probe of shock fronts and relativistic electrons produced during cluster mergers at high redshifts, that are hard to spatially resolve by current and near-future X-ray detectors. Quality of image reconstruction is poor with the 12m array alone but improved significantly by adding ACA; expected sensitivity of the 12m array based on the thermal noise is not valid for the Sunyaev-Zel'dovich effect mapping unless accompanied by an ACA observation of at least equal duration. The observations above 100 GHz will become excessively time-consuming owing to the narrower beam size and the higher system temperature. On the other hand, significant improvement of the observing efficiency is expected once Band 1 is implemented in the future.

Key words: cosmology: observations – galaxies: clusters: – radio continuum: galaxies – techniques: interferometers

1. Introduction

The Sunyaev-Zel'dovich effect (SZE, Sunyaev & Zel'dovich 1972), inverse Compton scattering of the cosmic microwave background off hot electrons, provides a unique probe of the intracluster medium (for reviews see Rephaeli 1995; Birkinshaw 1999; Carlstrom, Holder & Reese 2002). For the gas with given electron density n_e and temperature T_e at redshift z, surface brightness of the thermal SZE is proportional to the line-of-sight integral of electron density times temperature, $\int n_e T_e dl$, whereas that of the X-ray thermal bremsstrahlung emission is proportional to $(1+z)^{-4} \int n_e^2 T_e^{1/2} dl$. The relative significance of the SZE over the X-ray emission thus increases with redshift and electron temperature. This makes the SZE a powerful tool in detecting the shocks and the hot gas associated with violent cluster mergers (Kitayama et al. 2004; Ota et al. 2008; Korngut et al. 2011), the frequency of which is expected to increase at high redshifts when the growth of cosmic structures was faster than today.

As of today, however, spatial resolutions of the majority of the SZE images are at arcminute scales with a limited number of exceptions (Komatsu et al. 1999, 2001; Pointecouteau et al. 2001; Mason et al. 2010; Zemcov et al. 2010; Massardi et al. 2010; Korngut et al. 2011). This is largely due to the low surface brightness of the SZE and a small number of radio telescopes with sub-arcminute resolution in the range of wavelengths relevant to the SZE measurements. Controlling systematics of such large telescopes to the sensitivity level required for the SZE imaging is also challenging. Interferometers are therefore a promising and complementary tool for high sensitivity SZE imaging observations (e.g., Jones et al. 1993; Carlstrom, Joy & Grego 1996; AMI Collaboration 2006; Muchovej et al. 2007; Wu et al. 2009). Since it measures synchronized and correlated signals among different telescopes, an interferometer has a much better control of systematic noise, e.g., from the atmosphere. The obtained data also span

a wide range of spatial scales, making it possible to separate point-like sources from the SZE. On the other hand, it often has a limited field-of-view of $0.5' \sim 2'$ in the millimeter/submillimeter bands and requires a large number of pointings (or mosaics) to uncover the bulk of the cluster emission that extends over several arcminutes. The sensitivity also varies with spatial scales depending on observing conditions such as array configuration. Addition of single-dish data further improves the sensitivity for extended sources (e.g., Vogel et al. 1984; Stanimirovic et al. 1999; Takakuwa et al. 2003; Kurono, Morita & Kamazaki 2009). It is hence not always easy to know a priori to what extent a specific interferometer can be used to image the SZE within a realistic observing time.

In this paper, we investigate the feasibility of SZE imaging observations by the Atacama Large Millimeter/submillimeter Array (ALMA).[1] ALMA will consist of at least 66 antennas, designed to operate at photon frequencies between 30 GHz and 950 GHz. A major array of 12-meter antennas will be combined with the Atacama Compact Array (ACA, Iguchi et al. 2009) made up of 7-meter antennas and 12-meter single-dish antennas to improve the spatial frequency coverage and the total power measurement. While the inclusion of ACA should greatly enhance the capability of ALMA in observing extended sources, the practical feasibility and how to optimize it with such heterogeneous arrays in real observations are not straightforward and certainly depend on the nature of the target. We thus perform detailed imaging simulations of the SZE observations with ALMA including ACA using their latest configurations (see Pety, Gueth & Guilloteau 2001; Helfer et al. 2002; Pfrommer, Ensslin & Sarazin 2005; Takakuwa et al. 2008 for earlier imaging simulations of different targets).

We pay particular attention to resolving the shock structures of distant merging clusters that are relatively compact and hence suit the field-of-view of ALMA. We take the so-called bullet cluster, 1E 0657-558 at $z = 0.296$, as a representative example and perform mock observations using snap shots of state-of-the-art numerical simulations for this cluster (Takizawa 2005; Akahori & Yoshikawa 2012). 1E 0657-558 is well known for its prominent bow shock observed by Chandra (Markevitch et al. 2002) with the inferred Mach number of 3.0 ± 0.4 and the shock velocity of ~ 4700 km s^{-1} (Markevitch & Vikhlinin 2007). It has also been observed frequently via the SZE (e.g., Andreani et al. 1999; Halverson et al. 2009; Plagge et al. 2010; Zemcov et al. 2010; Malu et al. 2010). The temperature or the energy distribution of the shocked electrons, however, is still poorly constrained even for this well-observed cluster because of the lack of sensitivity of current X-ray and SZE detectors. We will show that ALMA is a powerful instrument capable of resolving a merger shock structure of galaxy clusters at high redshifts and improving our understanding of cluster evolution.

Throughout the paper, we assume a standard set of cosmological parameters: $\Omega_m = 0.27$, $\Omega_\Lambda = 0.73$, and $h =$
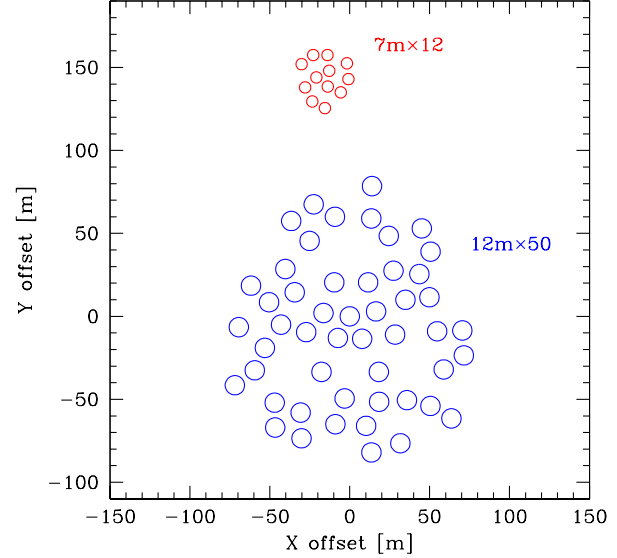

Fig. 1. The compact array configuration of 12m×50 and 7m×12 used in our mock observations. The projected positions on the UTM coordinate are shown with the symbol sizes representing the diameters of the telescopes.

0.70 (Komatsu et al. 2011). In this cosmology, an angular size of $1''$ corresponds to a physical size of 4.4 kpc and 8.1 kpc at $z = 0.3$ and $z = 1$, respectively.

2.   Imaging Simulations

The imaging simulations are performed using the MIRIAD software (Sault, Teuben & Wright 1995), version 4.2.3. Following the currently planned specifications of ALMA, we consider an array made up of fifty 12-meter antennas (hereafter 12m×50) and ACA made up of twelve 7-meter antennas (hereafter 7m×12) and four 12-meter single-dish antennas (hereafter SD×4). A summary of telescope specifications are given in Table 1.

To maximize the sensitivity for the extended signals, the most compact array configurations, shown in Figure 1, are adopted for 12m×50 and 7m×12.[2] The simulations are performed at 90GHz, which is the lowest frequency (and hence has the largest field-of-views and the lowest system temperature) in the initially planned specifications of ALMA. This frequency is also expected to be an optimal choice for the SZE observation owing to the minimal contamination by synchrotron and dust emissions. The prospects for the observations in the other bands will be discussed in §4.

2.1.   Input Models

We use three input models whose observational set-ups are summarized in Table 2. For each of the model images, we adopt the pixel size of $1''$, to satisfy the Nyquist condition for the smallest spatial scale, $\sim 3''$ full width at

---

[2]   The antenna configuration files are identical to alma.out01.cfg and aca.i.cfg used in CASA 3.3.

Table 1. Summary of telescope parameters.

Number of antennas	12m×50, 7m×12, SD×4
Configuration	Most compact
Frequency	90 GHz (Band 3)
Bandwidth	7.5 GHz per polarization
Intermediate frequency	6 GHz
System temperature	73.5 K
Aperture efficiency	0.71
Correlator efficiency	0.88
Primary beam FWHM	69″ (12m×50), 118″ (7m×12)
Phase error (rms)	20°
Gain error (rms)	0.1%
Pointing error (rms)	0.6″

half maximum (FWHM), probed by the longest baseline of ALMA at 90GHz in the most compact configuration. Wherever necessary, linear interpolation is performed to assign the intensity to each pixel. The model images are created to cover the entire observing area.

2.1.1. Model A: Gaussian

The first model is a simple two dimensional Gaussian, placed at zenith $(\mathrm{RA},\mathrm{DEC}) = (00:00:00, -23:00:00)$, with FWHM ranging from 5″ to 60″. The peak intensity is fixed at $-100\mu\mathrm{Jy}/\mathrm{arcsec}^2$, corresponding to the Compton y-parameter of 5×10^{-3} at 90GHz. We use this model simply to examine how the feasibility depends on the source size when the noises are negligible.

2.1.2. Model B: Bullet cluster

The second model is a latest result of 3D hydrodynamic simulations of a cluster merger by Akahori & Yoshikawa (2012) that are designed to reproduce the observed properties of the bullet cluster, 1E 0657-558. They carried out a set of N-body and SPH simulations of a collision of two galaxy clusters with virial masses of 1.5×10^{15} and 2.5×10^{14} M$_\odot$ and the initial relative velocity of 3000 km s^{-1}, using a code developed by Akahori & Yoshikawa (2010). We use the result after 1.12 Gyr from the initial condition for their two temperature model and compute the intensity map of the SZE, including relativistic corrections (Itoh & Nozawa 2004; Nozawa, Itoh & Kohyama 2005). To improve the agreement with the existing data, we renormalize the electron density so that the peak y-parameter ($\propto n_e T_e$) matches the central value of 3.31×10^{-4} inferred by APEX-SZ (Halverson et al. 2009). This is realized by reducing the electron density in each mesh by 26%.[3] To cover both the SZ emission peak and the shock front, the image center is shifted by $-15''$ (66 kpc) and $+20''$ (88 kpc) along the right ascension and declination, respectively, from that plotted in Figs 1–6 of Akahori & Yoshikawa (2012) and placed at $(\mathrm{RA},\mathrm{DEC}) = (6:58:27.4, -55:56:50)$. As the spatial resolution of the simulation is moderate near the shock

front (26 kpc or 6.0″), we use this model mainly to examine the feasibility of observing the global structure of a real cluster.

To further examine the feasibility of separating radio sources from the SZE, we add to Model B point sources in the field of 1E 0657-558 reported in the literature (Liang et al. 2000; Wilson et al. 2008; Malu et al. 2010). The source flux at 90GHz is estimated by the following procedure; i) wherever available, we extrapolate the observed fluxes at the two nearest frequencies to 90GHz assuming a single power-law, ii) if the observed flux is available only at one frequency, we extrapolate it assuming a single power-law with a spectral index of -0.5, iii) to be conservative against uncertainties in the extrapolation, we multiply the extrapolated fluxes by a factor of 2. The resulting source properties are listed in Table 3.

2.1.3. Model C: Shock front

The third model is based on a higher spatial resolution Eulerian mesh simulations of a moving substructure within a main cluster by Takizawa (2005). The model used in this paper is nearly the same as "the radial infall model" in Takizawa (2005) except that the gas density is reduced by a factor of 10 so that the y-parameter around the shock front matches that of Model B. We compute the SZE map from a snapshot at the elapsed time of 0.78 Gyr from the start of the simulation, which roughly reproduces the observed morphology of 1E 0657-558, and place it at $(\mathrm{RA},\mathrm{DEC}) = (6:58:17.3, -55:56:30)$. This model predicts the y-parameter gap across the shock front of 1.5×10^{-4}, about half the central y-parameter of this cluster. As this simulation has a higher spatial resolution (2 kpc or 0.5″) and a smaller box size (0.8 Mpc or 180″) than Akahori & Yoshikawa (2012), we use Model C to examine the feasibility of resolving a merger shock in a cluster. As our mock observations are performed on a slightly larger area than the box size of Takizawa (2005), we pad mirror images to the original simulation output to cover the entire observing area.

2.2. Mock visibilities

Mock interferometric observations are performed over the sky area of $120'' \times 120''$ (Models A and C) or $240'' \times 240''$ (Model B). Linear mosaicing (e.g., Sault, Staveley-

---

[3]   Reducing only the electron density yields the most conservative estimate of the predicted SZE intensity for a given y-parameter, because the relativistic correction leads to the larger reduction in the predicted intensity for the higher electron temperature at 90GHz.

Table 2. Summary of model parameters.

Parameter	Model A	Model B	Model C
RA (J2000)	$00:00:00$	$6:58:27.4$	$6:58:17.3$
DEC (J2000)	$-23:00:00$	$-55:56:50$	$-55:56:30$
Hour Angle	-1 hr ~ 1 hr	-5 hr ~ 5 hr	-5 hr ~ 5 hr
Mapping area			
12m×50, 7m×12	$120'' \times 120''$	$240'' \times 240''$	$120'' \times 120''$
SD×4	$190'' \times 190''$	$310'' \times 310''$	$190'' \times 190''$
Pixel size			
12m×50, 7m×12	$1''$	$1''$	$1''$
SD×4	$10''$	$10''$	$10''$
Number of mosaics/pointings			
12m×50	19	67	19
7m×12	7	23	7
SD×4	400	1024	400
Total integration time			
12m×50	2 hr	10 hr	10 hr
7m×12, SD×4	2 hr	40 hr	40 hr
Noise added			
12m×50, 7m×12	thermal	thermal, phase gain, pointing	thermal, phase gain, pointing
SD×4	thermal	thermal	thermal
Synthesized beam (major, minor, p.a.)*			
12m×50	$4.0''$, $3.8''$, $-7.3°$	$4.9''$, $4.2''$, $-88°$	$4.8''$, $4.2''$, $-88°$
7m×12	$17''$, $16''$, $5.1°$	$19''$, $18''$, $83°$	$19''$, $18''$, $84°$
12m×50+7m×12	$4.1''$, $3.8''$, $-7.3°$	$5.2''$, $4.6''$, $-88°$	$5.2''$, $4.5''$, $-88°$
SD×4	$69''$, $69''$, $0°$	$69''$, $69''$, $0°$	$69''$, $69''$, $0°$
Thermal noise (μJy/arcsec^2, μJy/beam)†			
12m×50	1.1, 19	0.62, 15	0.35, 8.0
7m×12	0.48, 150	0.15, 60	0.099, 38
12m×50+7m×12	1.0, 18	0.52, 14	0.30, 7.8
SD×4	0.64, 3400	0.23, 1200	0.14, 770

* Three numbers for each model denote the major axis FWHM, the minor axis FWHM, and the position angle, respectively.
† Two numbers for each model denote the rms values in μJy/arcsec^2 and μJy/beam, respectively.

Smith & Brouw 1996) is performed with pointing centers lying on triangular grids separated by half the primary beam FWHM given in Table 1. Each mosaicing center is observed repeatedly for 30 sec on-source and 5 sec toward an off-source calibrator with a sampling interval of 5 sec. The numbers of mosaics, the hour angles, and the total integration times are listed in Table 2. The target elevation is above $20°$ throughout the hour angles considered in this paper. As shown in Appendix 1, effective integration time toward each sky point apart from the map edge is nearly uniform and given by

$$t_{\rm eff} \simeq 2.6 \frac{t_{\rm int}}{N_{\rm mos}}, \qquad (1)$$

where $t_{\rm int}$ is the total integration time, $N_{\rm mos}$ is the number of mosaics, and the numerical factor accounts for the overlap of mosaics for the grid orientation mentioned above.

The visibility data are then created separately for 12m×50 and 7m×12 by performing the 2D Fourier transformation to the $u-v$ plane using the MIRIAD task *uvgen* and *uvmodel*. The visibility loss due to shadowing by adjacent telescopes is also taken into account. The thermal noise is computed in all models using the same param-

eters as the ALMA sensitivity calculator [4] as of March 2012; the system temperature, the aperture efficiency, the correlator efficiency, the bandwidth, and the intermediate frequency are listed in Table 1. The system temperature is computed by adopting the source declination of Model B ($-55:56:50$) and precipitable water vapour of 2.748 mm at 90GHz.

For Models B and C, antenna phase and gain noises with rms values of 20 degrees and 0.1%, respectively, are also added over an interval of 5 minutes using the MIRIAD task *gperror*. Relative pointing errors are also added to these models in an approximate manner by convolving the input images by a Gaussian with $0.6''$ rms before creating the visibilities. This would be sufficient for our present purpose because the pointing errors practically affect our results only via identifications of point sources and the $u-v$ coverage of ALMA is very good as shown below.

Figure 2 illustrates the $u-v$ coverage of our mock observations. The spatial frequencies that correspond to the baseline lengths from 4 to 48 kλ and 2 to 10 kλ are covered

---

Table 3. Positions and fluxes of model point sources.

Input			Reconstructed		
ΔR.A.[arcsec]	ΔDec [arcsec]	Flux [mJy]	ΔR.A.[arcsec]	ΔDec [arcsec]	Flux [mJy]
83	-12	1.0	83	-12	0.93
89	-35	0.74	89	-35	0.69
-108	147	0.47	-108	147	0.42*
144	86	0.45	144	86	0.43*
117	-111	0.43	117	-111	0.37
-68	-111	0.37	-68	-111	0.31
78	113	0.16	79	113	0.14
-95	-94	0.13	-95	-94	0.14
-25	97	0.079	-25	97	0.092
-30	9	0.035			undetected
54	-68	0.032			undetected
1	44	0.028			undetected

* Sources lying outside the $240'' \times 240''$ region mapped by 12m$\times$50.

nearly uniformly by 12m$\times$50 and 7m$\times$12, respectively, where $\lambda = 3.3$ mm at 90GHz. Properties of the resulting synthesized beams are given in Table 2. The effective area of the synthesized beam is given by

$$A_{\mathrm{beam}} = \frac{2\pi\theta_{\mathrm{beam}}^2}{8\ln 2} = 28 \ \mathrm{arcsec}^2 \left(\frac{\theta_{\mathrm{beam}}}{5''}\right)^2, \qquad (2)$$

where θ_{beam} is the geometric mean of the major axis FWHM and the minor axis FWHM.

In addition, single-dish images are created in real space assuming a Gaussian beam with 69$''$ FWHM and taking account of the thermal noise. An additional factor of $\sqrt{2}$ is multiplied to the thermal noise level so as to take account of beam switching. Since the spatial resolution of the single-dish data is considerably worse than that of 12m$\times$50 and 7m$\times$12, the single-dish mapping is performed over a larger sky area to reduce the edge effect; an extra 35$''$ (0.5 FWHM) guard band is observed on each side of the image to cover $190'' \times 190''$ (Models A and C) or $310'' \times 310''$ (Model B). As the primary beams of 12m$\times$50 and 7m$\times$12 also extend into the guard band, we will be able to detect point sources in this band to some extent as will be shown in §3.2. The pixel size of the single-dish image is taken to be 10$''$ (Table 2). While this somewhat oversamples the data, we adopt this pixel size in the present analysis for the following reasons; i) as the expected random noise of the single-dish image reduces linearly with the pixel size, the above choice serves as a conservative limit, ii) the thermal noise of the single-dish data in μJy/arcsec^2 is already smaller than that of 12m$\times$50 with the above pixel size (Table 2), and iii) we find that adopting larger pixel sizes often results in spurious distortions in the reconstructed images after deconvolved jointly with the interferometric data. Yen et al. (2011) also show that one may well reproduce the extended emission by adopting pixel sizes that are sufficiently smaller than the primary beam of an interferometer. Effective integration time at each point of the single-dish image, including the time spent for beam switching, is given by

$$t_{\mathrm{eff,SD}} = \frac{t_{\mathrm{int,SD}}}{N_{\mathrm{point,SD}}}, \qquad (3)$$

where $t_{\mathrm{int,SD}}$ is the total integration time and $N_{\mathrm{point,SD}}$ is the number of pointings of SD$\times$4 listed in Table 2.

The mock data so obtained are reduced without a priori knowledge of the input model or point sources as described in the following subsections. The point source removal and image deconvolution are both performed over the extended regions with the guard band mentioned above. Impacts of other sources of noise than considered here will be discussed in §3.4.

2.3. Point source removal

Whenever point sources are present, we make use of long baseline data to remove them before reconstructing the extended emission. First, a dirty map and a dirty beam are created only for 12m$\times$50 by an inverse Fourier transformation of mock visibilities using the MIRIAD task *invert*.

Second, the position and the apparent flux of a source whose peak brightness lies above a certain threshold value are identified with the CLEAN algorithm by Steer, Dewdney & Ito (1984) using the MIRIAD task *mossdi*. If there are multiple sources, the flux of each source may be mutually influenced via the side-lobe effects. A single point source may also be detected as a superposition of separate sources. In either case, the apparent flux of the i-th source can be expressed as

$$F_i^{\mathrm{app}} = \sum_{j=1}^{N} S_{ij} F_j^{\mathrm{int}}, \qquad (4)$$

where N is the total number of detections, F_j^{int} is the intrinsic flux of the j-th source, and the matrix S_{ij} describes the contribution of F_j^{int} to F_i^{app} for a given beam shape and source positions. Given knowledge of the $u-v$ coverage of the observations, one can estimate the components of S_{ij} and solve the linear algebraic equations for F_j^{int}. In the present analysis, all the detections that lie within the synthesized beam FWHM from each other are

regarded as components of a single source, whose flux and position are given by the sum and the flux-weighted mean, respectively, of fluxes and positions of all the components.

Finally, contribution of identified sources is removed from the visibility data of both 12m×50 and 7m×12 as well as from the SD×4 image.

2.4. Image deconvolution

Having removed the identified point sources, we create dirty images and dirty beams for either each of or the combinations of 12m×50 and 7m×12. The Briggs robust weighting scheme (Briggs 1995) is adopted with the robustness parameter of 0.5. The dirty images are then deconvolved (corrected for the effects of the dirty beams and re-convolved with a Gaussian beam) with the Maximum Entropy Method (MEM), which is more suitable for the extended signals than CLEAN (e.g., Narayan & Nityananda 1986; Sault 1990). Non-linear deconvolution is applied using the MIRIAD task *mosmem* to the dirty images either separately or jointly with the single-dish image. Since the SZE brightness is negative at $\nu < 220$ GHz while MEM is applicable only to the positive signals, we change the sign of the entire maps when applying MEM. The pixel size is taken to be the same as the input image (1″).

Since a proper estimate of the underlying noise level of an image with an extended source is not straightforward, we adopt and compare the following two definitions using the pixels within $120″ × 120″$ (Models A and C) or $240″ × 240″$ (Model B); 1) $\sigma_{\rm th}$ is the rms value of a deconvolved image with the same observing parameters but using the *null* input model including only the thermal noise, and 2) $\sigma_{\rm diff}$ is the rms value of the difference map between the deconvolved output and the smoothed input; the input described in §2.1 is convolved by a Gaussian with the same FWHM as the synthesized beam of the output. The values of $\sigma_{\rm th}$ are given in Table 2. Thermal noise is nearly constant over the map except near the edge.

Finally, we quantify the quality of reconstruction by the image fidelity defined by (Pety, Gueth & Guilloteau 2001)

$$f(\vec{\theta}) \equiv \frac{|I_{\rm in}^{\rm smooth}(\vec{\theta})|}{\max\{|I_{\rm out}(\vec{\theta}) - I_{\rm in}^{\rm smooth}(\vec{\theta})|,\ 0.7\sigma_{\rm diff}\}} \quad (5)$$

where $I_{\rm out}(\vec{\theta})$ is the output intensity of the deconvolved image at a sky position $\vec{\theta}$ and $I_{\rm in}^{\rm smooth}(\vec{\theta})$ is the input intensity smoothed with the same synthesized Gaussian beam as the output. The above fidelity roughly corresponds to an inverse of the fractional error of reconstruction. The second term in the denominator is introduced to avoid an overshoot of the fidelity due to a coincidental match between the input and the output.

3. Results

3.1. Model A: Gaussian

We plot in Figure 3 the results of a representative case of a Gaussian model with $\theta_{\rm model} = 40″$ FWHM after total integrations of 2 hr 12m×50, 7m×12, and SD×4, respec-
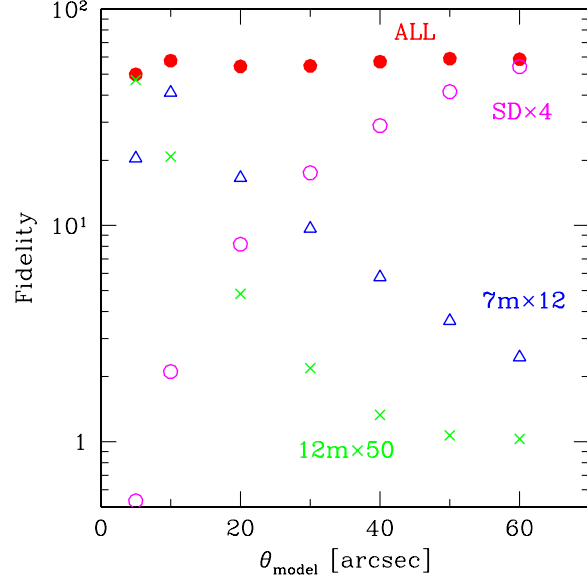

Fig. 4. Mean fidelity of the deconvolved images as a function of $\theta_{\rm model}$ for Model A. The mean is taken over the central $70″ × 70″$ and $\theta_{\rm model} × \theta_{\rm model}$ for SD×4 and the others, respectively. Symbols indicate the results for 12m×50 (crosses), 7m×12 (open triangles), SD×4 (open circles), and 12m×50 + 7m×12 + SD×4 (filled circles).

tively. With the 12m×50 data alone, reconstruction is poor and extended (≫ arcsec) feature is largely missed even though the noise level of the 12m×50 image (panel b) is ∼ 1/100 of the peak signal. This is also indicated by the fact that $\sigma_{\rm diff} \gg \sigma_{\rm th}$. On the other hand, significant improvement in the image fidelity is achieved once low spatial frequency data from 7m×12 and SD×4 are included (panels d, e, f). The brightness of the SD×4 image appears to be low simply because it is diluted by a large beam (panel c).

Figure 4 illustrates how the mean fidelity around the center varies with the spatial extent of the emission. It is evident that the interferometric data lose sensitivity for the emission much more extended than the size of their synthesized beams, i.e., $\theta_{\rm beam} \sim 5″$ for 12m×50 and $\theta_{\rm beam} \sim 20″$ for 7m×12. The single-dish data play an essential role in improving the sensitivity at larger scales.

3.2. Model B: Bullet cluster

Figure 5 shows the images of a simulated bullet cluster after total integrations of 10 hr for 12m×50 and 40 hr for 7m×12 and SD×4. We have fiducially fixed the ratio between the integration times at its nominal value of 1:4 (Pety, Gueth & Guilloteau 2001; Morita & Holdaway 2005). The impact of changing the ratio will be discussed in §3.5.

The morphology of the input SZE image (Fig. 5a) is quite different from that in X-rays plotted in Figure 1 of Akahori & Yoshikawa (2012). In particular, the so-called "bullet", the X-ray peak of the sub-cluster, is not apparent in the SZE image as it lies near the contact discontinuity
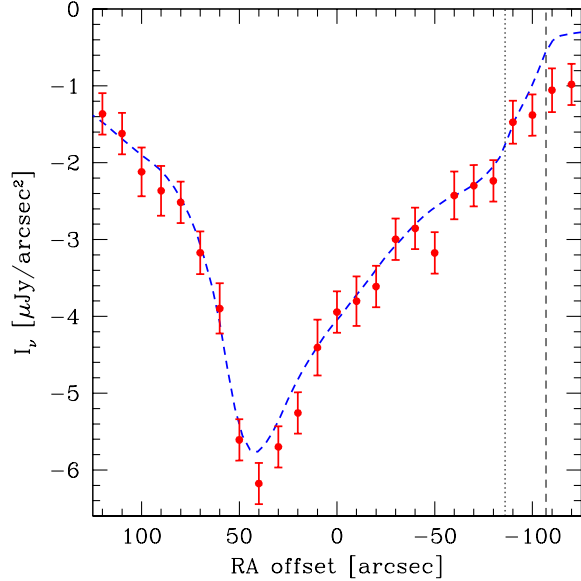
Fig. 6. Comparison of the input model (thick dashed line) and the mock data (error bars) for Model B over a strip with width $10''$ shown in Figure 5(e). The bin size is $10''$. The vertical lines indicate the positions of the shock front (thin dashed) and the contact discontinuity (thin dotted), respectively, on the collision plane of the two merging clusters.

across which pressure is nearly constant. On the other hand, the shock front, i.e., the pressure gap, ahead of the bullet is more prominent (see also Figs 6 and 8) and extends over several hundred kpc. The SZE peak lies near the X-ray peak of the main cluster where electron density and temperature are both high.

There are 12 radio point sources over $310'' \times 310''$ among which 10 lie within the $240'' \times 240''$ region mapped by 12m×50 (Fig. 5a). All the sources brighter than ~ 0.1 mJy are detected above a conservative threshold of 7 $\sigma_{\rm th}$ in the 12m×50 data as indicated in Table 3 and Figure 5(b). After correcting for the side-lobe effects as described in §2.3, reconstructed fluxes agree with the input values within 20% for the resolved point sources and the source positions are identified more accurately. While the aperture bias of the source fluxes has been enhanced by pointing errors, it is still comparable to the thermal noise and we do not attempt to correct it further in the present paper. Two bright sources in the guard band are also detected, although the noise level there is larger due to the primary beam attenuation beyond the map edge. The remaining 3 fainter sources are undetected but their contamination to the SZE is negligible.

Once the detected sources are removed, the deconvolved image by 12m×50 + 7m×12 + SD×4 reproduces the input model with the maximum fidelity reaching ~ 16 (panels e and f in Fig. 5). The fact that $\sigma_{\rm th} \simeq \sigma_{\rm diff}$ holds also assures that the reconstruction of the extended signal is as good as expected.

Figure 6 further illustrates one-dimensional SZE intensity profile across the shock front. The error bars indicate

the statistical error of the mean in each bin estimated by

$$\sigma_{\rm bin} = \frac{1}{\sqrt{N_{\rm beam}}} \max(\sigma_{\rm std},\ \sigma_{\rm th}), \qquad (6)$$

where $\sigma_{\rm std}$ is the standard deviation of the pixel data in the bin and $N_{\rm beam} = A_{\rm bin}/A_{\rm beam}$ is the number of synthesized beams contained in the bin area $A_{\rm bin}$. In equation (6), we use $N_{\rm beam}$, instead of the number of pixels, because the pixel values in a deconvolved image are correlated over the beam area $A_{\rm beam}$. Note also that $\sigma_{\rm bin}$ does not include explicitly the thermal noise of the single-dish data (see Table 2) that is responsible for fluctuations on spatial scales larger than $A_{\rm bin}$. It is evident from this figure that the overall structure of this cluster is well reconstructed, although the shock front is only marginally resolved. We therefore explore the feasibility of a targeted observation toward the shock below.

3.3.   Model C: Shock front

We plot in Figure 7 the images toward the shock front after total integrations of 10 hr for 12m×50 and 40 hr for 7m×12 and SD×4. Again, reconstruction is significantly improved by adding the short baseline data of 7m×12 and SD×4.

Figure 8 shows that the high angular resolution SZE observation with ALMA is a powerful tool to resolve the shock front, characterized by the temperature and pressure jumps. On the other hand, the X-ray emission is weak in the low-density shock region and rises sharply behind the contact discontinuity. The Compton y-parameter or projected pressure is nearly constant behind the contact discontinuity (a slight disagreement between its peak and the contact discontinuity is due to the projection effect). The SZE and X-rays are thus complementary in probing the detailed shock structure and the former is particularly useful in detecting hot rarefied gas.

The width of the shock heated region is ~ 60 kpc corresponding to $\sim 14''$ at $z = 0.3$ as displayed in Figure 8 or $\sim 8''$ at $z = 1$. This physical size is consistent with the X-ray data of this cluster presented in Figure 32 of Markevitch & Vikhlinin (2007), whereas the errors in the inferred X-ray spectroscopic temperatures are still large. Given the fact that the intensity of the SZE is redshift independent and the angular diameter distance is nearly constant at $z > 1$, our results strongly point to the good capability of ALMA in resolving shocks at such high redshifts.

3.4.   Systematic errors of the single-dish data

As noted in §3.1, single-dish data play an essential role in reconstructing the extended signals. Due to a larger beam size and a smaller number of antennas, the single-dish data are likely to be affected more severely by systematic errors, such as calibration errors and atmospheric fluctuations, than the interferometric data. To check the impacts of uniform and random systematic uncertainties, we re-run the mock observations of Model C by i) reducing the SD×4 gain by 20% or ii) enhancing the random noise of the SD×4 data by an order of magnitude. For the latter,
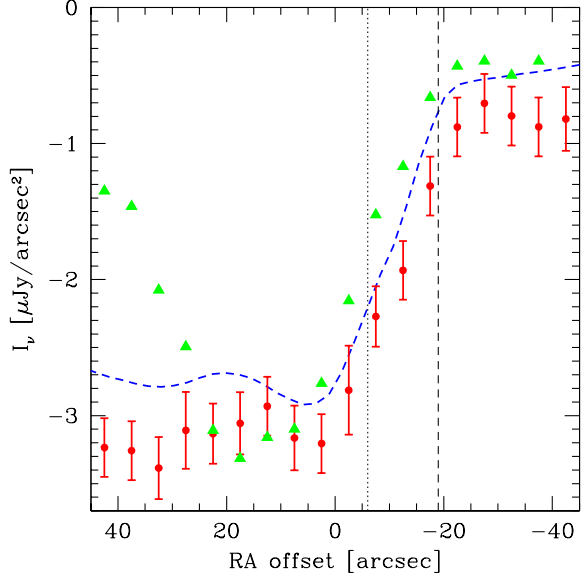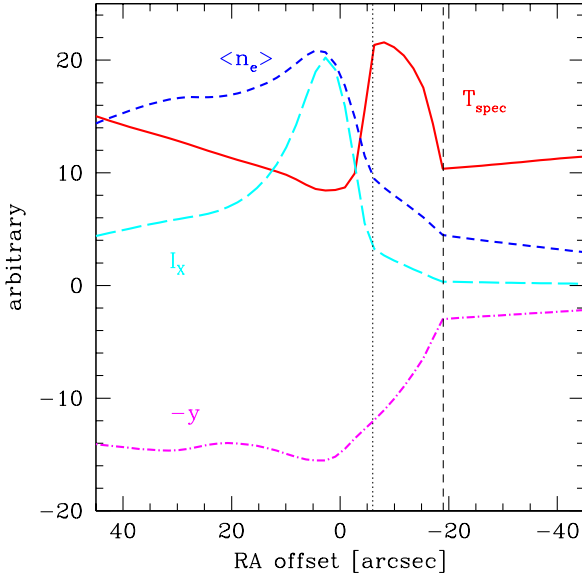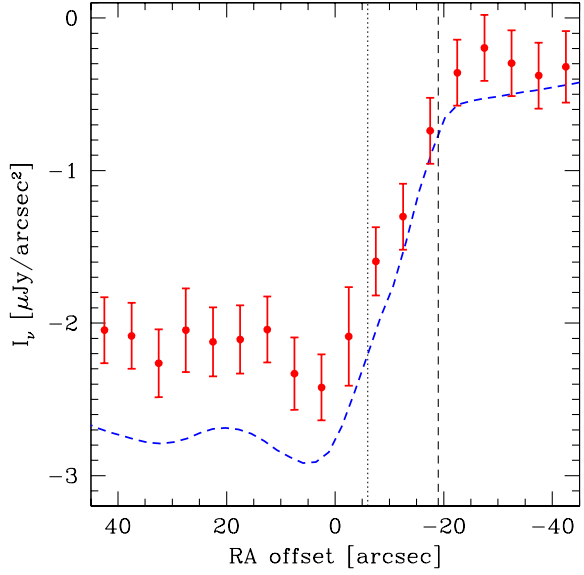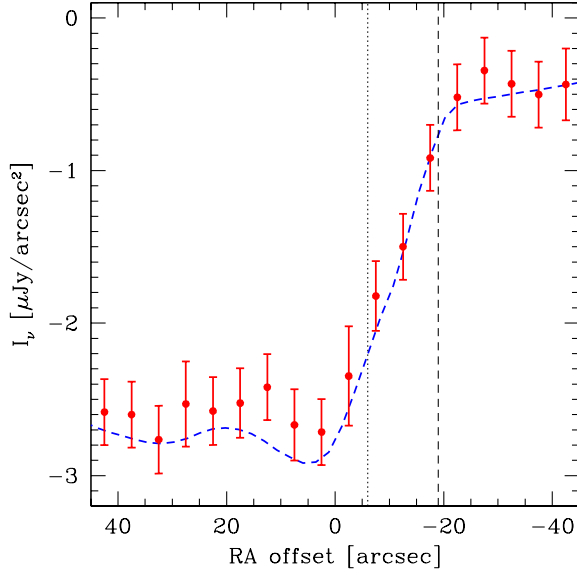
Fig. 8. *Top:* Same as Fig. 6 except that the results of Model C shown in Fig. 7(e) are plotted with a smaller bin size of 5″. *Bottom:* Physical quantities with arbitrary units of the input model for the same region as plotted in the top panel. Thick lines indicate the projected temperature proposed by Mazzotta et al. (2004) that mimics the X-ray spectroscopic temperature (solid), the mass weighted electron density (short dashed), the thermal bremsstrahlung X-ray brightness (long dashed), and the Compton y-parameter with a negative sign added for comparison with the SZE decrement (dot-dashed).

Fig. 9. Same as the top panel of Fig. 8 except for introducing a systematic reduction in the single-dish gain by 20% (top) or additional random noise on the single-dish data that is an order of magnitude larger than the thermal noise (bottom). Triangles in the bottom panel show the results of the linear method of combining the single-dish data (error bars are omitted for clarity). Error bars do not explicitly include the single-dish noise as described in the text.

we also examine a linear method, often called feathering, to combine the single-dish data instead of non-linear joint deconvolution; a deconvolved image is produced only for 12m×50+7m×12 by MEM and then combined with the SD×4 image using the MIRIAD task *immerge*.

Figure 9 shows that introducing a reduction in the single-dish gain by $\sim 20\%$ results in a systematic decrease

in the reconstructed brightness by $\sim 20\%$ as well. On the other hand, the enhanced random noise primarily leads to an offset in the zero brightness level, whereas the shape of the emission profile is nearly unchanged. The latter bias has been known as an intrinsic problem with MEM for low S/N data (e.g., Cornwell, Braun & Briggs 1999). The linear method described above gives a better estimation of the zero level but poorer results on the emission profile (bottom panel). This is because the linear method
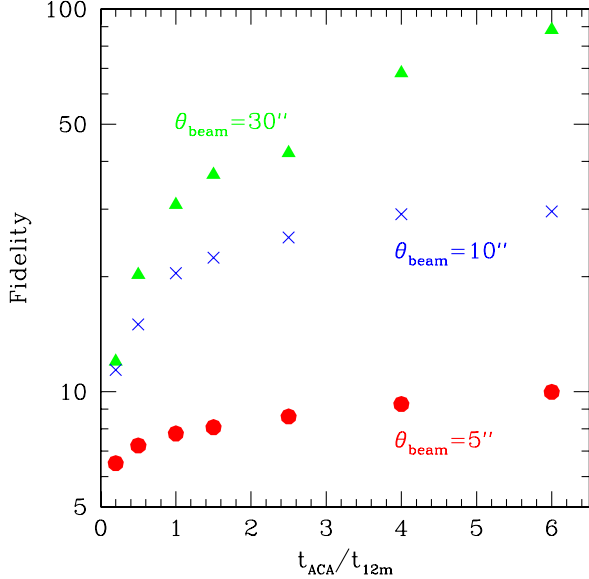
Fig. 10. Mean fidelity of the mock bullet cluster (Model B without point sources) as a function of the integration time of ACA (7m×12 and SD×4). The integration time of 12m×50 is fixed at 10 hr. The mean is taken within the central $60'' \times 60''$ in the 12m×50 + 7m×12 + SD×4 image without smoothing (circles) or after being smoothed to the effective beam FWHM of $10''$ (crosses) and $30''$ (triangles).

directly combines the single-dish data with the interferometer data on the $u - v$ plane and hence retains noisy pixel values in the single-dish map. On the other hand, MEM searches for a smooth solution that accounts for the global structure of the single-dish data and is less sensitive to individual pixel values. In either case, the above results suggest that the quality of the SD×4 data may limit the accuracy of the SZE observations.

3.5. Relative integration time between the 12m array and ACA

In Models B and C, the ratio between the integration times of 12m×50 and ACA (7m×12 and SD×4) has been taken at its nominal value of $t_{\rm ACA}/t_{\rm 12m} = 4$ (Pety, Gueth & Guilloteau 2001; Morita & Holdaway 2005). We now examine the impacts of varying this ratio by re-running wide-field Model B simulations. The total integration time of 12m×50 is fixed at 10 hr and the point sources are excluded from the input for simplicity.

Figure 10 indicates that $t_{\rm ACA}/t_{\rm 12m} \gtrsim 1$ is required to achieve a $\sim 10\%$ accuracy in the image reconstruction at the resolution of 12m×50, $\theta_{\rm beam} \sim 5''$. For smaller $t_{\rm ACA}/t_{\rm 12m}$, the thermal noise of ACA in μJy/arcsec^2 dominates over that of 12m×50, as can be readily expected from Table 2. For larger $t_{\rm ACA}/t_{\rm 12m}$, on the other hand, the image fidelity increases more rapidly at larger scales. The optimal value of $t_{\rm ACA}/t_{\rm 12m}$ thus depends on the spatial scale of interest, and the nominal value of 4 appears to be a reasonable choice for the case considered in the present paper.

4. Discussion

High resolution SZE mapping with ALMA has profound implications on cosmology and structure formation. First of all, the shock velocity inferred via the Rankine-Hugoniot jump condition from Chandra for 1E 0657-558 amounts to ~ 4700 km s^{-1} (Markevitch & Vikhlinin 2007), which appears to be exceptionally high within the framework of a concordance ΛCDM model (e.g., Hayashi & White 2006; Lee & Komatsu 2010). Our results suggest that ALMA can significantly improve both quality and quantity of such studies by detecting shocks up to $z > 1$ and measuring directly the pressure gap across the shock.

The existence of very hot electrons with $kT_{\rm e} \gg 10$ keV in clusters has also been inferred by the past SZE observation (Kitayama et al. 2004) and the hard X-ray spectroscopy (Ota et al. 2008; Nakazawa et al. 2009; Sugawara, Takizawa & Nakazawa 2009). Nevertheless their spatial distribution as well as the link to the non-thermal component are still unclear. ALMA will be highly complementary in probing the nature of these relativistic electrons to hard X-ray missions such as NuSTAR[5] and ASTRO-H[6], whose spatial resolutions are $45''$ and $1.7'$, respectively.

Our results can further be used to estimate the feasibility of SZE observations in other bands. Frequency dependence of the SZE maps will provide a useful probe of line-of-sight gas motions via the kinematic SZE, electron temperature via relativistic corrections, and the existence of non-thermal electrons (e.g., Colafrancesco, Marchegiani & Buonanno 2011; Prokhorov et al. 2011). The SZE increment at frequencies above 600 GHz has also been detected by Herschel toward 1E0657-558 (Zemcov et al. 2010).

For given arrays and bandwidths, the thermal noise in Jy/sr is proportional to $T_{\rm sys}t_{\rm int}^{-1/2}\nu^2$, where $T_{\rm sys}$ is the system temperature, $t_{\rm int}$ is the integration time and ν is the observing frequency. If one is to observe a source of intensity $I_{\rm src}$ in Jy/sr with $N_{\rm mos}$ mosaics and perform smoothing over $N_{\rm sm}$ beams, the signal-to-noise ratio is given by

$$\frac{S}{N} \propto \frac{|I_{\rm src}|t_{\rm int}^{1/2}}{T_{\rm sys}\nu^2}\frac{N_{\rm sm}^{1/2}}{N_{\rm mos}^{1/2}}. \tag{7}$$

Given that both $N_{\rm mos}$ and $N_{\rm sm}$ are nearly proportional to ν^2 for fixed observing area and effective beam size after smoothing, the integration time to reach a given signal-to-noise ratio is

$$t_{\rm int} \propto \frac{T_{\rm sys}^2\nu^4}{|I_{\rm src}|^2}. \tag{8}$$

Figure 11 shows the quantity given in equation (8) in the cases of the thermal SZE with $kT_{\rm e} = 15$ keV and the kinematic SZE with the line of sight velocity of $V = 3000$ km s^{-1}, including relativistic corrections (Itoh & Nozawa 2004; Nozawa, Itoh & Kohyama 2005). The vertical axis shows the ratio with respective to the integration time for the thermal SZE at 90GHz. We use system temperatures

---

[5]   http://www.nustar.caltech.edu/
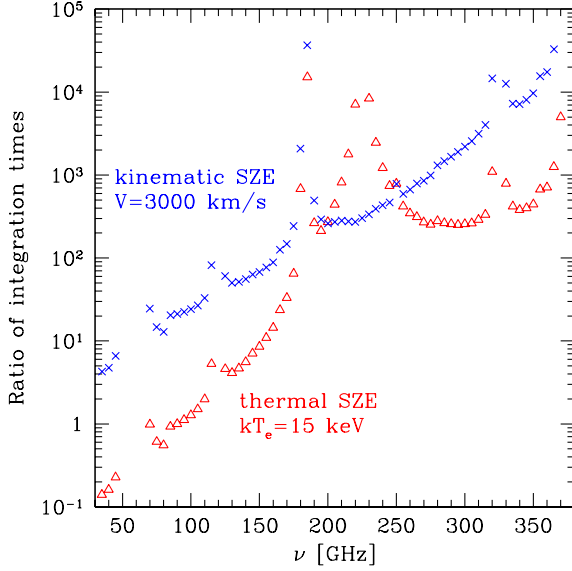[6]   http://astro-h.isas.jaxa.jp/

Fig. 11. The ratio of integration times, as a function of observing frequency, required to reach a given signal-to-noise ratio in a fixed effective spatial resolution over a fixed observing area. Symbols indicate the cases for the thermal SZE with $kT_e = 15$ keV (triangles) and the kinematic SZE with $V = 3000$ km s^{-1} (crosses). The vertical axis is normalized with respective to the integration time for the thermal SZE at 90GHz.

at zenith $(\mathrm{RA}, \mathrm{DEC}) = (00:00:00, -23:00:00)$ given by the ALMA sensitivity calculator. Precipitable water vapour is taken to be 2.748 mm at $\nu < 163$ GHz, 1.796 mm at $163 \le \nu < 275$ GHz, and 1.262 mm at $275 \le \nu < 500$ GHz. The resulting system temperatures tend to increase gradually from $T_{\mathrm{sys}} \sim 40$ K at $\nu \sim 40$ GHz to $T_{\mathrm{sys}} \sim 180$ K at $\nu \sim 350$ GHz, with some overshoots wherever atmospheric opacity gets high, e.g., at $\nu \sim 180$ GHz. The rise of the integration time for the thermal SZE at $\nu \sim 220$ GHz is due to the null of its intrinsic spectrum. It is obvious that the SZE observations, particularly that of the kinematic SZE, become highly time-consuming at $\nu > 100$GHz due both to an increasing T_{sys} and to the ν^4 factor in equation (8). On the other hand, much faster mapping is possible at lower frequencies, e.g., $\nu = 40$ GHz.

Finally, we estimate the impact of unresolved (< 0.1 mJy) point-like sources as follows. The 150GHz source counts from recent SPT and ACT observations are approximately $N(> S_\nu) \sim 2 \times 10^{-4} (S_{150}/10\mathrm{mJy})^{-1}$ arcmin^{-2} for synchrotron-dominated sources and $N(> S_\nu) \sim 10^{-5}(S_{150}/10 \mathrm{\ mJy})^{-2.5}$ arcmin^{-2} for dust-dominated sources at $S_{150} \sim 10$ mJy (Vieira et al. 2010; Marriage et al. 2011). If we simply extrapolate these relations to fainter fluxes at 90 GHz, the nominal confusion criterion of $1/30$ beam^{-1}, or equivalently 4 arcmin^{-2} for $\theta_{\mathrm{beam}} = 5''$, is reached at $S_{90} \sim 0.6$ μJy and 10 μJy, assuming the average spectral shapes of $S_\nu \propto \nu^{-0.5}$ and ν^3 for the two populations (e.g., Vieira et al. 2010), respectively. This suggests that the source confusion is not likely to affect severely the SZE observations considered in this paper,

unless there is a significant excess of faint sources with respect to the above extrapolation.

5. Conclusions

We have performed imaging simulations of the SZE of galaxy clusters with ALMA including ACA. In its most compact configuration at 90GHz, ALMA will resolve the intracluster medium with an effective angular resolution of $\sim 5''$, corresponding to ~ 20 kpc at $z = 0.3$ and ~ 40 kpc at $z = 1$. Such observations will be particularly useful in detecting shock fronts and/or relativistic (either thermal with $kT_e \gg 10$ keV or non-thermal) electrons produced during violent cluster mergers at high redshifts, that are hard to resolve by current and near-future X-ray detectors.

Our results imply that ACA plays an essential role in reconstructing the global structures of the SZE and its capability may be limited by the accuracy of single-dish data. Expected sensitivity of the 12m array based on the thermal noise is not valid for the SZE mapping unless accompanied by an ACA observation of at least equal duration. An optimal ratio of integration times between the two observations depends on the spatial scale of interest and the nominal value of 4 appears to be a reasonable choice in the present case. The SZE observations at $\nu > 100$GHz will become excessively time-consuming owing to the narrower beam size and the larger system temperature. On the other hand, significant improvement of the observing efficiency is expected once Band 1 is implemented in the future.

In addition to the SZE, ALMA will detect radio/IR sources in the field-of-view. The spectral energy distributions of such sources in the ALMA bands are still highly uncertain and will be crucial both in understanding the nature of the sources and in quantifying their contamination to the SZE survey data (e.g., Lin et al. 2009).

Note Added in Proof (June 22, 2012)

After this paper was accepted for publication, updates to the ALMA sensitivity calculator released on May 31, 2012 resulted in an increase in the system temperature at

90GHz by 10% and an inclusion of quantization efficiency of 0.96, compared to those listed in Table 1. These modifications would simply raise the thermal noise amplitude by 14% and the results of the present paper remain essentially unchanged once the quoted integration times are scaled upward by 30%.

Appendix 1. Effective Integration Time in Mosaicing Observations

In mosaicing observations, effective integration time toward a given sky position $\vec{\theta}$ is expressed as

$$t_{\rm eff}(\vec{\theta}) = \epsilon_{\rm m}^2(\vec{\theta})\frac{t_{\rm int}}{N_{\rm mos}}, \tag{A1}$$

where $t_{\rm int}$ is the total integration time over the entire mapping area, $N_{\rm mos}$ is the number of mosaics, and $\epsilon_{\rm m}(\vec{\theta})$ is the "mosaicing overlap factor" introduced in Holdaway & Rupen (1995) and Morita & Holdaway (2005). The last quantity accounts for the overlap of mosaics that cover the same position $\vec{\theta}$ and is given by

$$\epsilon_{\rm m}^2(\vec{\theta}) = \sum_{p=1}^{N_{\rm mos}} g^2(\vec{\theta} - \vec{\theta}_p), \tag{A2}$$

where g is the primary beam gain and $\vec{\theta}_p$ is the pointing center of the p-th mosaic. In what follows, we derive the values of $\langle\epsilon_{\rm m}^2\rangle$ and $\langle t_{\rm eff}\rangle$ analytically.

First, we consider primary beam gain functions of the form

$$g(\theta) = \begin{cases} \exp\left(-\frac{\theta^2}{2\sigma_{\rm G}^2}\right) & \text{Gaussian}, \\ \left[\frac{2J_1(\pi D\theta/\lambda)}{\pi D\theta/\lambda}\right]^2 & \text{Airy disk}, \end{cases} \tag{A3}$$

where J_1 is the Bessel function of the the first kind of order unity, D is the diameter of the telescope, and λ is the observing wavelength. Integrating g^2 over the sky gives the effective area of integration per pointing as

$$A_{\rm gain} = \begin{cases} \pi\sigma_{\rm G}^2 \simeq 0.567\,\theta_{\rm pb}^2 & \text{Gaussian}, \\ \frac{2^5\lambda^2 I_A}{\pi D^2} \simeq 0.554\,\theta_{\rm pb}^2 & \text{Airy disk}, \end{cases} \tag{A4}$$

where

$$I_A \equiv \int_0^\infty \frac{J_1(x)^4}{x^3}dx \simeq 0.0575, \tag{A5}$$

and $\theta_{\rm pb}$ is the primary beam FWHM corresponding to $\sqrt{8\ln 2}\sigma_{\rm G}$ for Gaussian and $1.028\lambda/D$ for the Airy disk. For each p in equation (A2), $g^2 \sim 1$ within $A_{\rm gain}$ centered at $\vec{\theta}_p$, whereas $g^2 \sim 0$ otherwise.

Second, we suppose that mosaicing centers are placed on a regular grid, either square or triangular, with constant spacing d. The physical area around each grid point enclosed by perpendicular bisectors with the neighboring points is

$$A_{\rm grid} = \begin{cases} d^2 & \text{square grid}, \\ \frac{\sqrt{3}}{2}d^2 & \text{triangular grid}, \end{cases} \tag{A6}$$

where the shape of the enclosed area is a square and a hexagon, respectively.

Finally, we average equation (A2) around an arbitrary grid point $\vec{\theta}_q$ that lies sufficiently far ($\gg \sqrt{A_{\rm gain}/\pi}$) from the map edge, to obtain

$$\langle\epsilon_{\rm m}^2\rangle = \frac{\sum_{p=1}^{N_{\rm mos}} \int_q g^2(\vec{\theta} - \vec{\theta}_p)d^2\theta}{\int_q d^2\theta}$$

$$= \frac{\sum_{p=1}^{N_{\rm mos}} \int_p g^2(\vec{\theta} - \vec{\theta}_q)d^2\theta}{\int_q d^2\theta} = \frac{A_{\rm gain}}{A_{\rm grid}}, \tag{A7}$$

where $\int_i$ denotes an integral around the i-th grid point over the area $A_{\rm grid}$. The last result in equation (A7) does not depend on q and remains unchanged even if the average is taken over multiple grids. Substituting equations (A4) and (A6) into (A7) yields

$$\langle\epsilon_{\rm m}^2\rangle = \langle\epsilon_{\rm m}^2\rangle_{\rm Ny}\left(\frac{d}{0.5\theta_{\rm pb}}\right)^{-2}, \tag{A8}$$

where the representative values in the case of Nyquist spacing are

$$\langle\epsilon_{\rm m}^2\rangle_{\rm Ny} \simeq \begin{cases} 2.27 & \text{Gaussian, square grid}, \\ 2.62 & \text{Gaussian, triangular grid}, \\ 2.22 & \text{Airy disk, square grid}, \\ 2.56 & \text{Airy disk, triangular grid}. \end{cases} \tag{A9}$$

Equations (A1) and (A7) give

$$\frac{\langle t_{\rm eff}\rangle}{t_{\rm int}} = \frac{\langle\epsilon_{\rm m}^2\rangle}{N_{\rm mos}} \sim \frac{A_{\rm gain}}{A_{\rm map}}, \tag{A10}$$

where $N_{\rm mos}A_{\rm grid}$ roughly equals the mapping area $A_{\rm map}$. Equation (A10) indicates that the *mean* integration time at each sky position within fixed $A_{\rm map}$ *does not* (apart from the time spent at the map edge) depend on d or the grid orientation; $\langle\epsilon_{\rm m}^2\rangle$ and $N_{\rm mos}$ are both proportional to d^{-2}. On the other hand, its *dispersion does* as shown below.

We further compute numerically the mean and the standard deviation of $\epsilon_{\rm m}^2$ by creating square and triangular grids over the sky area with $5\theta_{\rm pb} \times 5\theta_{\rm pb}$ and extracting 10000 random positions of $\vec{\theta}$ from the central $3\theta_{\rm pb} \times 3\theta_{\rm pb}$. Figure 12 illustrates that $\Delta\epsilon_{\rm m}^2/\langle\epsilon_{\rm m}^2\rangle$, or equivalently $\Delta t_{\rm eff}/\langle t_{\rm eff}\rangle$, drops sharply to $\ll 1\%$ at $d < 0.5\theta_{\rm pb}$ in all the cases considered here. We have checked that $\langle\epsilon_{\rm m}^2\rangle$ computed numerically agrees with equations (A8) and (A9) to better than 1% and 4% at $d < 0.7\theta_{\rm pb}$ and $d < \theta_{\rm pb}$, respectively. The agreement improves further once the larger computational area is adopted.

The above results imply that, as far as the Nyquist condition is satisfied, square and triangular grids lead to practically similar and uniform effective integration time apart from the map edge. The difference due to assumed shapes of the primary beam, Gaussian or an Airy disk, is not significant either.

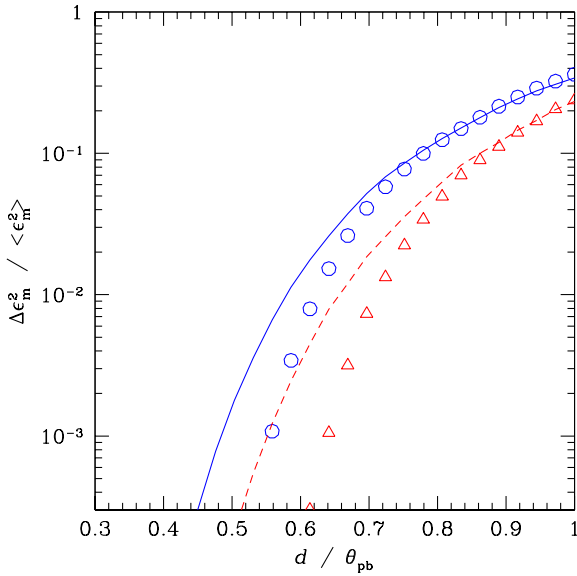## References

Akahori, T., & Yoshikawa, K. 2010, PASJ, 62, 335

Fig. 12. Standard deviation of the mosaicing overlap factor $\Delta\epsilon_m^2$ as a function of grid spacing d for a Gaussian primary beam on square (solid line) and triangular grids (dashed line) or an Airy-disk-shaped primary beam on square (circles) and triangular grids (triangles). The vertical and horizontal axes are normalized by the mean $\langle\epsilon_m^2\rangle$ and the primary beam FWHM θ_{pb}, respectively.

Akahori, T., & Yoshikawa, K. 2012, PASJ, 64, 12

AMI Collaboration: Barker, R., et al. 2006, MNRAS, 369, L1

Andreani, P., et al. 1999, ApJ, 513, 23

Birkinshaw, M. 1999, Phys. Rep. 310, 97

Briggs, D. S. 1995, PhD theses, New Mexico Tech.

Carlstrom, J. E., Holder, G. P., & Reese, E. D., 2002, ARA&A, 40, 643

Carlstrom, J. E., Joy, M., Grego, L. 1996, 456, L75

Colafrancesco, S., Marchegiani, P., & Buonanno, R. 2011, A&A, 527, L1

Cornwell, T., Braun, R., & Briggs, D. S. 1999, in ASP Conf. Ser. 180, Synthesis Imaging in Radio Astronomy II, ed. G. B. Taylor, C. L. Carilli, & R. A. Perley (San Francisco: ASP), 151

Muchovej, S., et al. 2007, ApJ, 663, 708

Halverson, N. W., et al. 2009, ApJ, 701, 42

Hayashi, E., & White, S. D. M. 2006, MNRAS, 370, L380

Helfer, T. T., Vogel, S. N., Lugten, J. B., & Teuben, P. J. 2002, PASP, 114, 793

Holdaway, M. A., & Rupen M. P. 1995, ALMA Memo 128

Iguchi, S., et al. 2009, PASJ, 61, 1

Itoh, N., & Nozawa, S. 2004, A&A, 417, 827

Jones, M., et al. 1993, Nature, 365, 320

Kitayama, T., Komatsu, E., Ota, N., Kuwabara, T., Suto, Y., Yoshikawa, K., Hattori, M., & Matsuo, H. 2004, PASJ, 56, 17

Komatsu, E., Kitayama, T., Suto, Y., Hattori, M., Kawabe, R., Matsuo, H., Schindler, S., & Yoshikawa, K. 1999, ApJ, 516, L1

Komatsu, E., et al. 2001, PASJ, 53, 57

Komatsu, E., et al. 2011, ApJS, 192, 18

Korngut, P. M., et al. 2011, ApJ, 734, 10

Kurono, Y., Morita, K., & Kamazaki, T. 2009, PASJ, 61, 873

Lee, J., Komatsu, E. 2010, ApJ, 718, 60

Liang, H., Hunstead, R. W., Birkinshaw, M., & Andreani, P. 2000, ApJ, 544, 686

Lin, Y.-T., Partridge, B., Pober, J. C., Bouchefry, K. E., Burke, S., Klein, J. N., Coish, J. W., Huffenberger, K. M., 2009, ApJ, 694, 992

Malu, S. S., Subrahmanyan, R., Wieringa, M., & Narasimha, D. 2010, arXiv:1005.1394

Markevitch, M., Gonzalez, A. H., David, L., Vikhlinin, A., Murray, S., Forman, W., Jones, C., Tucker, W. 2002, ApJ, 567, L27

Markevitch, M., & Vikhlinin, A., 2007, Physics Reports, 443, 1

Marriage, T. A., et al. 2011 ApJ, 731, 100

Massardi, M., Ekers, R. D., Ellis, S. C., Maughan, B. 2010, ApJ, 718, L23

Mason, B. S., et al. 2010, ApJ, 716, 739

Mazzotta, P., Rasia, E., Moscardini, L., & Tormen, G. 2004, MNRAS, 354, 10

Morita, K., & Holdaway, M. A. 2005, ALMA Memo 538

Nakazawa, K., et al. 2009, PASJ, 61, 339

Narayan, R., & Nityananda, R. 1986, ARA&A 24, 127

Nozawa, S., Itoh, N., Kohyama, Y. 2005, A&A, 440, 39

Ota, N., et al. 2008, A&A, 491, 363

Pety, J. , Gueth F., & Guilloteau, S. 2001, ALMA Memo 398

Pfrommer, C., Ensslin, T. A., & Sarazin, C. L. 2005, A&A, 430, 799

Plagge, T., et al. 2010, ApJ, 716, 1118

Pointecouteau, E., Giard, M., Benoit, A., Désert, F. X., Bernard J.P., Coron, N., & Lamarre, J. M. 2001, ApJ, 552, 42

Prokhorov, D. A., Colafrancesco, S., Akahori, T., Million, E. T., Nagataki, S., Yoshikawa, K. 2011, MNRAS, 416, 302

Rephaeli, Y. 1995, ARA&A, 33, 541

Sugawara, C., Takizawa, M., & Nakazawa, K. 2009, PASJ, 61, 1293

Sault, R. J. 1990, ApJ, 354, L61

Sault, R. J., Staveley-Smith, L., & Brouw, W. N. 1996, A&AS, 120, 375

Sault R. J., Teuben P. J., & Wright M. C. H. 1995, In Astronomical Data Analysis Software and Systems IV, eds R. Shaw, H.E. Payne, J.J.E. Hayes, ASP Conference Series, 77, 433

Steer, D. G., Dewdney, P. E., & Ito, M. R. 1984, A&A, 137, 159

Stanimirovic, S., Staveley-Smith, L., Dickey, J. M., Sault, R. J., Snowden, S. L. 1999, MNRAS, 302, 417

Sunyaev, R. A., & Zel'dovich, Ya. B. 1972, Comments Astrophys. Space Phys., 4, 173

Takakuwa, S., Kamazaki, T., Saito, M., & Hirano, N. 2003, ApJ, 584, 818

Takakuwa, S., Iono, D., Vila-Vilaro, B., Sekiguchi, T., & Kawabe, R. 2008, Ap&SS, 313, 169

Takizawa, M. 2005, ApJ, 629, 791

Vieira, J. D., et al. 2010, ApJ, 719, 763

Vogel, S. N., Wright, M. C. H., Plambeck, R. L., & Welch, W. J. 1984, ApJ, 283, 655

Yen, H-W., Takakuwa, S., Ohashi, N. 2011, ApJ, 742, 57

Wilson, G. W., et al. 2008, MNRAS, 390, 1061

Wu, J-H. P., et al. 2009, ApJ, 694, 1619
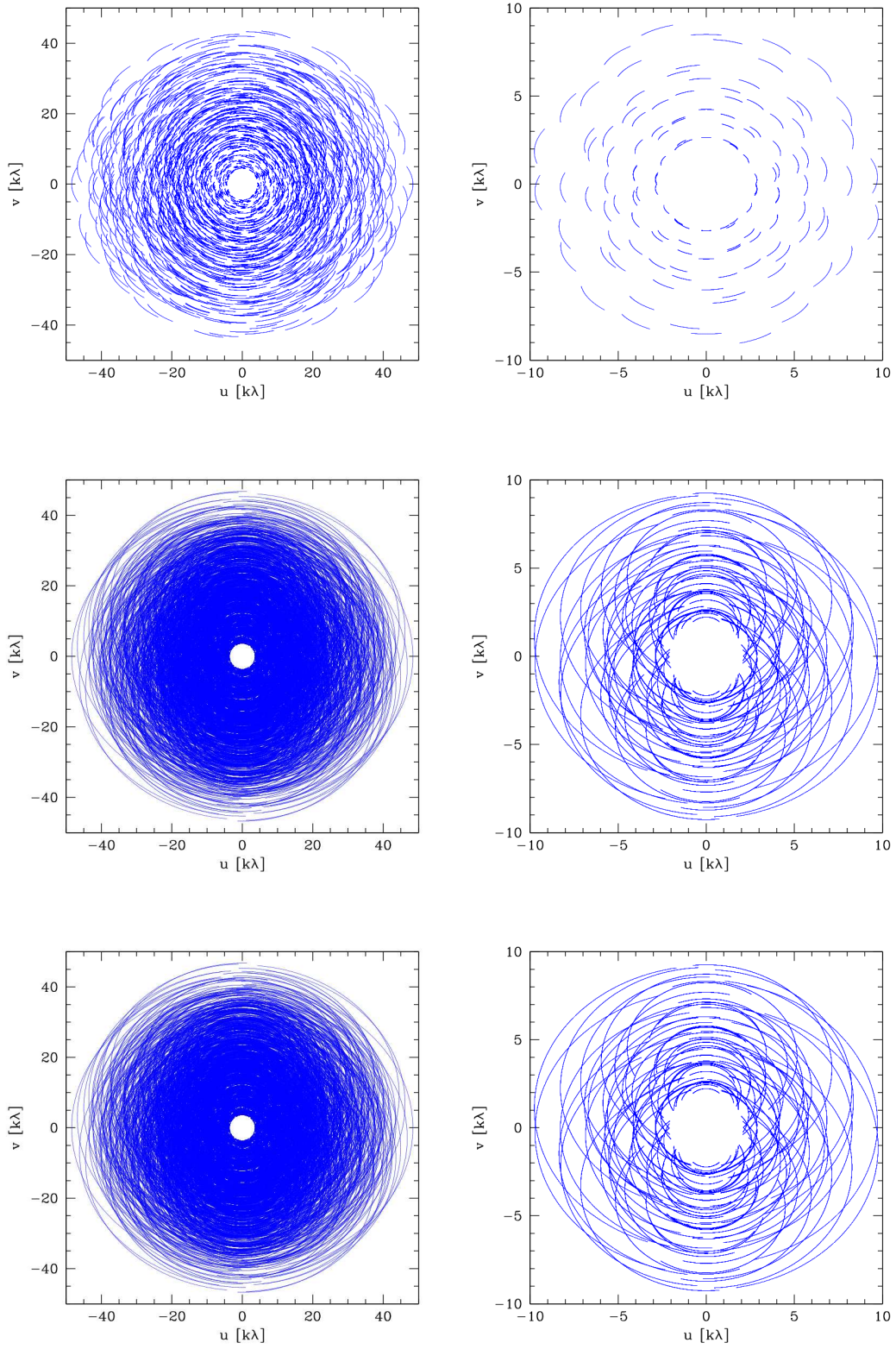
Zemcov, M., et al. 2010, A&A, 518, L16

Fig. 2. The $u-v$ coverages of our mock observations with 12m×50 (left) and 7m×12 (right) of Models A (top), B (middle), and C (bottom).
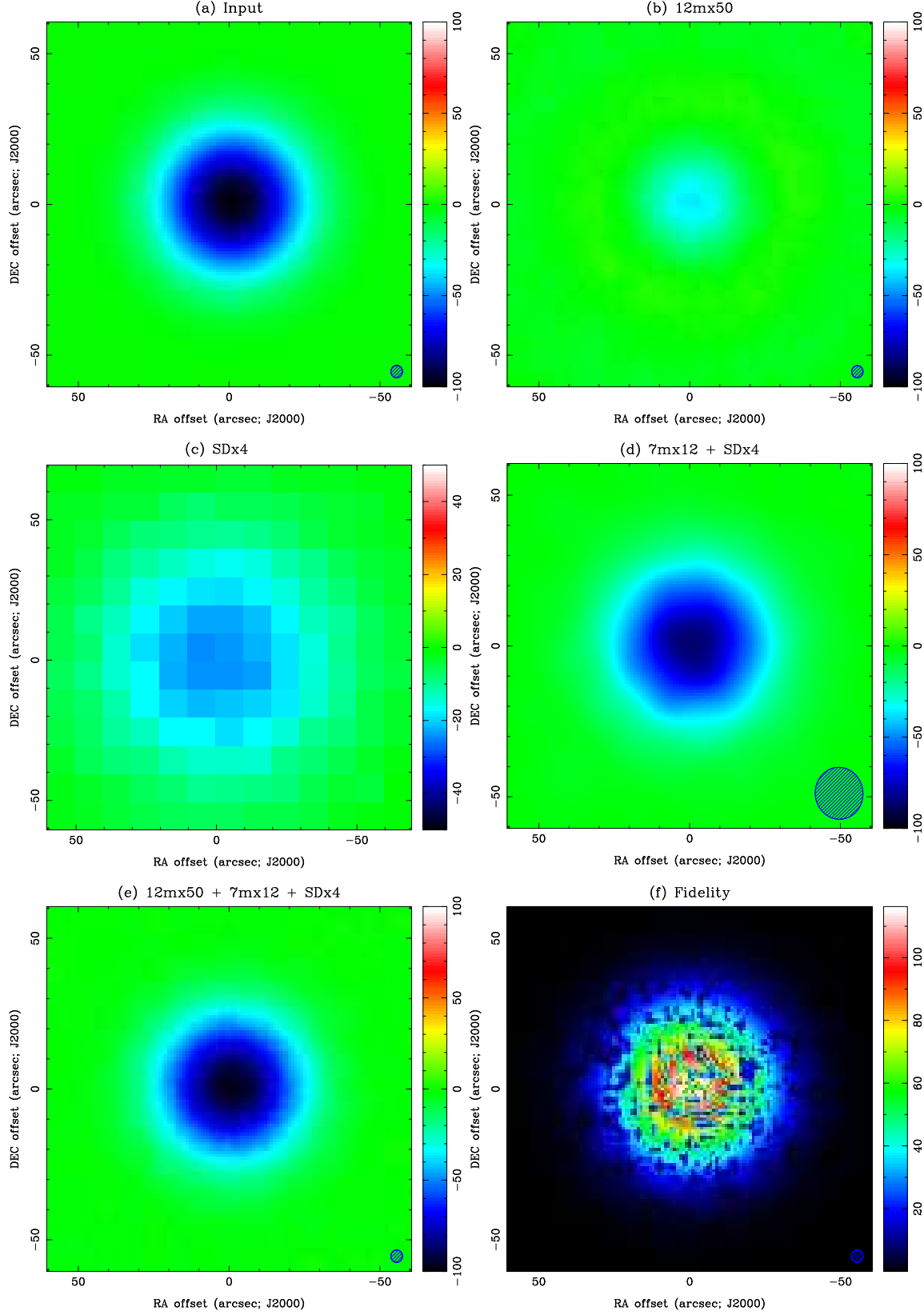
Fig. 3. Mock images of Model A (Gaussian) with $\theta_{\mathrm{model}} = 40''$. Except for panel (f), the color scale is in μJy/arcsec^2. A hatched ellipse at the bottom-right corner indicates the synthesized beam. (a) Input model convolved with the same synthesized beam as panel (e). (b) Deconvolved image for 12m×50 with $(\sigma_{\mathrm{th}}, \sigma_{\mathrm{diff}}) = (1.1, 17)$ [μJy/arcsec^2] and $\theta_{\mathrm{beam}} = 3.9''$. (c) SD×4 image with $\sigma_{\mathrm{th}} = 0.64$ μJy/arcsec^2 and $\theta_{\mathrm{beam}} = 69''$. (d) Deconvolved image for 7m×12 + SD×4 with $(\sigma_{\mathrm{th}}, \sigma_{\mathrm{diff}}) = (0.48, 0.79)$ [μJy/arcsec^2] and $\theta_{\mathrm{beam}} = 17''$. (e) Deconvolved image for 12m×50 + 7m×12 + SD×4 with $(\sigma_{\mathrm{th}}, \sigma_{\mathrm{diff}}) = (1.0, 1.2)$ [μJy/arcsec^2] and $\theta_{\mathrm{beam}} = 4.0''$. (f) Fidelity of the image shown in panel (e).
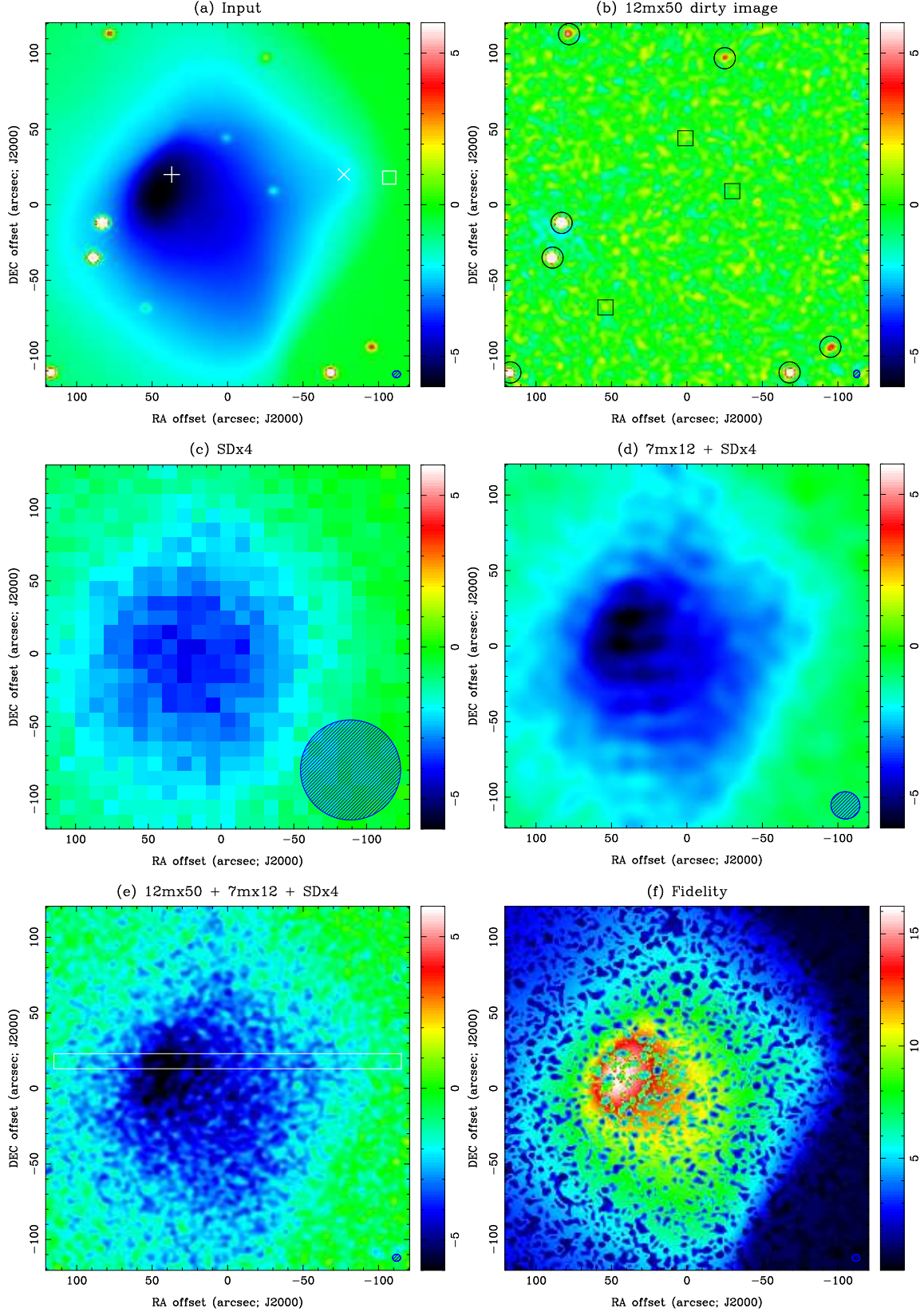
Fig. 5. Similar to Fig. 3 but for Model B (bullet cluster). (a) Input model convolved with the same synthesized beam as panel (e). Symbols indicate the positions of the X-ray peaks of the main cluster (plus) and the sub-cluster (cross), and the shock front (square). (b) Dirty image of 12m×50 with $\sigma_{\rm th} = 0.62$ μJy/arcsec^2 and $\theta_{\rm beam} = 4.5''$. Circles indicate the point sources that are detected and removed in the subsequent panels, whereas squares denote undetected ones. (c) SD×4 image with $\sigma_{\rm th} = 0.23$ μJy/arcsec^2 and $\theta_{\rm beam} = 69''$. (d) Deconvolved image for 7m×12 + SD×4 with $(\sigma_{\rm th}, \sigma_{\rm diff}) = (0.15, 0.18)$ [μJy/arcsec^2] and $\theta_{\rm beam} = 19''$. (e) Deconvolved image for 12m×50 + 7m×12 + SD×4 with $(\sigma_{\rm th}, \sigma_{\rm diff}) = (0.52, 0.53)$ [μJy/arcsec^2] and $\theta_{\rm beam} = 4.9''$. A box indicates the region over which the profile in Fig. 6 is computed. (f) Fidelity of the image shown in panel (e).
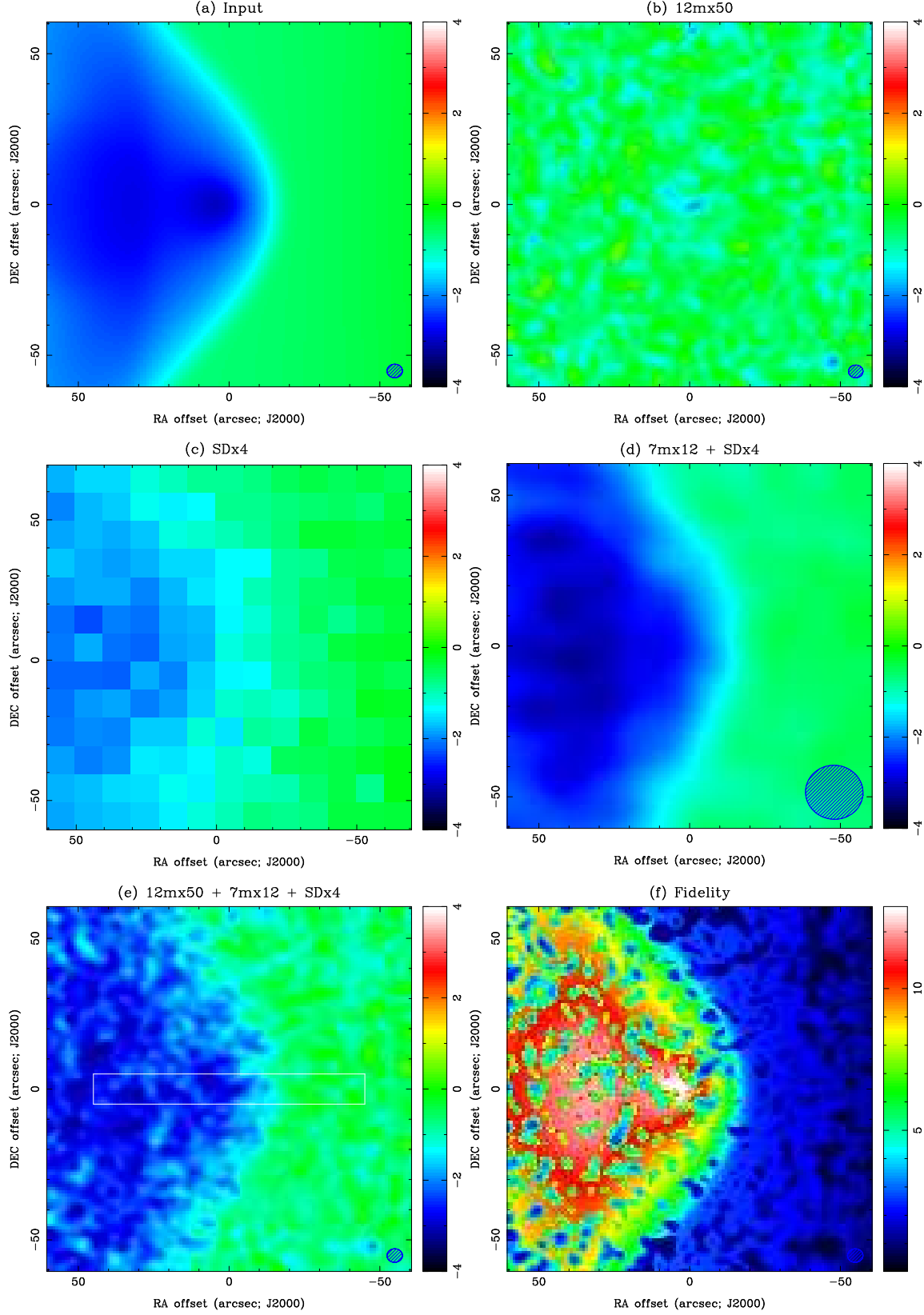
Fig. 7. Similar to Fig. 3 but for Model C (shock front). (a) Input model convolved with the same synthesized beam as panel (e). (b) Deconvolved image for 12m×50 with $(\sigma_{\mathrm{th}}, \sigma_{\mathrm{diff}}), = (0.35, 0.95)$ [μJy/arcsec^2] and $\theta_{\mathrm{beam}} = 4.5''$. (c) SD×4 image with $\sigma_{\mathrm{th}} = 0.14$ μJy/arcsec^2 and $\theta_{\mathrm{beam}} = 69''$. (d) Deconvolved image for 7m×12 + SD×4 with $(\sigma_{\mathrm{th}}, \sigma_{\mathrm{diff}}), = (0.099, 0.18)$ [μJy/arcsec^2] and $\theta_{\mathrm{beam}} = 18''$. (e) Deconvolved image for 12m×50 + 7m×12 + SD×4 with $(\sigma_{\mathrm{th}}, \sigma_{\mathrm{diff}}) = (0.30, 0.33)$ [μJy/arcsec^2] and $\theta_{\mathrm{beam}} = 4.8''$. A box indicates the region over which the profile in Fig. 8 is computed. (f) Fidelity of the image shown in panel (e).